NANO LETTERS
Cite This: Nano Lett. XXXX, XXX, XXX−XXX
Letter
pubs.acs.org/NanoLett

Stable Thiophosphate-Based All-Solid-State Lithium Batteries through Conformally Interfacial Nanocoating

Daxian Cao,[†,∥] Yubin Zhang,[‡,∥] Adelaide M. Nolan,[§] Xiao Sun,[†] Chao Liu,[†] Jinzhi Sheng,[†] Yifei Mo,[*,§] Yan Wang,[*,‡] and Hongli Zhu[*,†]

[†]Department of Mechanical and Industrial Engineering, Northeastern University, Boston, Massachusetts 02115, United States
[‡]Department of Mechanical Engineering, Worcester Polytechnic Institute, Worcester, Massachusetts 01609, United States
[§]Department of Materials Science and Engineering, University of Maryland, College Park, Maryland 20742, United States

Supporting Information

ABSTRACT: All-solid-state lithium batteries (ASLBs) are promising for the next generation energy storage system with critical safety. Among various candidates, thiophosphate-based electrolytes have shown great promise because of their high ionic conductivity. However, the narrow operation voltage and poor compatibility with high voltage cathode materials impede their application in the development of high energy ASLBs. In this work, we studied the failure mechanism of Li_6PS_5Cl at high voltage through in situ Raman spectra and investigated the stability with high-voltage $LiNi_{1/3}Mn_{1/3}Co_{1/3}O_2$ (NMC) cathode. With a facile wet chemical approach, we coated a thin layer of amorphous $Li_{0.35}La_{0.5}Sr_{0.05}TiO_3$ (LLSTO) with 15−20 nm at the interface between NMC and Li_6PS_5Cl. We studied different coating parameters and optimized the coating thickness of the interface layers. Meanwhile, we studied the effect of NMC dimension to the ASLBs performance. We further conducted the first-principles thermodynamic calculations to understand the electrochemical stability between Li_6PS_5Cl and carbon, NMC, LLSTO, NMC/LLSTO. Attributed to the high stability of Li_6PS_5Cl with NMC/LLSTO and outstanding ionic conductivity of the LLSTO and Li_6PS_5Cl, at room temperature, the ASLBs exhibit outstanding capacity of 107 mAh g^{-1} and keep stable for 850 cycles with a high capacity retention of 91.5% at C/3 and voltage window 2.5−4.0 V (vs Li−In).

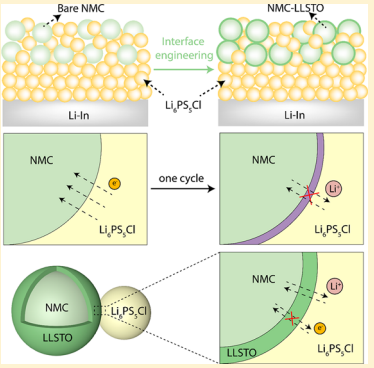

KEYWORDS: *Thiophosphate, interface engineering, stability, high-voltage cathode, nanocoating, all solid-state batteries*

Safety concerns of conventional lithium ion batteries (LIBs) with organic liquid electrolyte have increased due to their flammability and frequently reported accidents.[1,2] All-solid-state lithium batteries (ASLBs) have been considered as a solution to effectively address the safety issue.[3] Furthermore, when matched with Li metal anode, ASLBs are expected to have much higher energy density than the state-of-the-art LIB (<260 Wh kg^{-1}).[4,5] Therefore, ASLBs has attracted broad attention from academia to industry and government agencies.[6] In particular, highlighted with ionic conductivity comparable with liquid electrolyte and high mechanical deformability, thiophosphate-based solid-state electrolytes (SEs) are one of the most promising electrolytes for high-energy ASLBs working at room temperature.[5,7] In contrast, most reported ASLBs using polymer- and oxide-based SEs still need external heating or adding liquid electrolyte to achieve optimal behavior.[8,9]

To achieve high-energy-density batteries, layered $LiNi_{1/3}Mn_{1/3}Co_{1/3}O_2$ (NMC) is one of the most attractive cathode candidates due to high working potential (>3.6 V), promising capacity (∼160 mAh g^{-1}), relatively high electron conductivity (∼10^{-5} S cm^{-1}), and Li-ion diffusivity (∼10^{-11} cm^2 s^{-1}).[10,11] However, thiophosphate-based electrolytes suffer from severe interfacial instability with NMC cathode in ASLBs which leads to significant capacity loss, poor power density, and short cycling life.[12,13] The poor interface stability is caused by a narrow thermodynamic intrinsic electrochemical stability window of sulfide SE ranging from 1.7 to 2.3 V (versus Li^+/Li) and the tendency for the NMC cathode to oxidize the sulfide electrolyte in physical contact, in particular at high charging potential.[14,15] These thermodynamically favorable reactions decompose the solid electrolyte into passivated products with poor ionic conductivity, which causes significant interfacial resistance. Electronically conductive additives mixed into the cathode accelerate this decomposition.[16,17] The irreversible reaction causes a high initial capacity loss and low Coulombic efficiency.[18] Consequently, the energy and power density has been significantly limited.

To resolve this incompatibility issue between sulfide SEs and high-energy oxide cathodes, a thin protective oxide coating layer, such as $LiNbO_3$, $Li_4Ti_5O_{12}$, Li_2SiO_3, and Li_3PO_4, is employed to avoid the direct contact of SE and cathode.[19−23]

Received: July 1, 2019
Revised: September 17, 2019
Published: September 23, 2019

DOI: 10.1021/acs.nanolett.9b02678
Nano Lett. XXXX, XXX, XXX−XXX

Although this oxide coating can stabilize the interfaces, current interlayer materials often possess relative poor ionic conductivity ranging from 10^{-9} to 10^{-6} S cm^{-1} and require expensive coating techniques such as pulsed laser deposition (PLD).[24] A key challenge for high-energy ASLBs is to develop a novel buffer layer with higher ionic conductivity. Meanwhile, a scalable coating approach is highly desired to ensure a stable interface with fast interfacial conductivity.

Herein, we report a highly scalable and effective interface engineering on a high-energy cathode NMC with a thin amorphous $Li_{0.35}La_{0.5}Sr_{0.05}TiO_3$ (LLSTO) solid electrolyte layer to stabilize the NMC−thiophosphate SEs interface, achieving ASLBs with an outstanding voltage window, high capacity, and the longest known cycling performance to date. The LLSTO with ionic conductivity of 8.4×10^{-5} S cm^{-1} at 30 °C is in situ coated to the NMC surface via wet chemical method. The argyrodite Li_6PS_5Cl with high room-temperature ionic conductivity of $\sim 2 \times 10^{-3}$ S cm^{-1} is selected as the sulfide SE. The degradation of Li_6PS_5Cl at high oxidation voltage is in situ investigated through the Raman spectroscopy. In ASLBs with/without interface engineering, the interface stability and reaction kinetics are also studied, combined with the first-principles thermodynamic calculations. As a result, the thiophosphate-based ASLBs exhibit an outstanding voltage window with the longest cycling number so far.

Results and Discussion. Figure 1 schematically illustrates the basic configuration of ASLBs, the interface failure

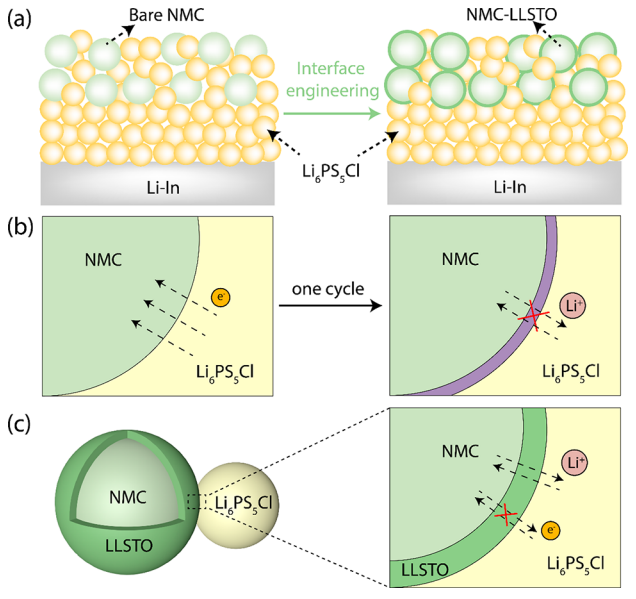

Figure 1. Schematic of (a) the configuration of ASLBs with/without interface engineering; (b) failure mechanism at the interface in bare NMC-based ASLBs; (c) interface stabilization with LLSTO layer.

mechanism between NMC and Li_6PS_5Cl electrolyte, and the interface stabilization with well-designed interface engineering. Bulk-type ASLBs with layered architecture are assembled, as shown in Figure 1a. The cathode layer is composed with active material (bare NMC or NMC coated with LLSTO (NMC-LLSTO)) and SE with no conductive additives. To avoid the interface reaction between Li and SEs, Li−In is utilized as the anode material. In ASLBs without engineering, Li_6PS_5Cl is directly in contact with NMC (Figure 1b). In the initial charge process, NMC oxidized Li_6PS_5Cl at high oxidation voltage and formed poor ionic−conductive products at the interface. This passivated layer leads to a huge capacity loss and sluggish reaction kinetics which limits the power density of the ASLBs. Therefore, a high ionic−conductive but electronic−insulate LLSTO layer was introduced at the interface between NMC and Li_6PS_5Cl, as illustrated in Figure 1c. The LLSTO layer is stable with NMC and has a higher oxidation potential. The insulation between NMC and Li_6PS_5Cl could avoid the degradation of Li_6PS_5Cl, which stabilize the Li_6PS_5Cl to higher voltage. Meanwhile, the outstanding ionic conductivity of LLSTO and intimate contact between NMC and Li_6PS_5Cl enable enhanced reaction kinetics.

The preparation of NMC-LLSTO is a typical wet-chemical method, which is illustrated in Figure 2a. Briefly, NMC powders were first soaked in the precursor solution of LLSTO with sufficient mixing. After the gel formation, NMC with homogeneous gel coating was collected. Followed by sintering in the air, the residual organic precursor was removed and a thin layer of LLSTO was formed at the NMC surface. The gel-forming process is vital for achieving a conformal coating (Figure S4). The thickness of the coating layer was well adjusted by controlling the ratio of NMC to LLSTO precursor. As depicted in Figure S5 and Table S1, a conformal coating on NMC is fabricated when the amount of LLSTO is lower than 0.5 mmol in 2.0 g NMC. When further increasing the concentration, a large impurity appeared, which can be concluded as the formation of the crystallized LLSTO. Scanning electron microscopy (SEM) was used to investigate the morphology of NMC before (Figure 2b) and after coating (Figure 2c). It is clear that a thin amorphous layer uniformly covered the surface of NMC particles. Figure 2d gives the X-ray diffraction signals of pure LLSTO, bare NMC, and NMC-LLSTO. Compared with high crystallinity of NMC, LLSTO exhibits weak and broadened peaks, which indicates its amorphous state. As a result, all peaks in NMC-LLSTO are indexed to the NMC, and there are no new phases detected, which suggests the LLSTO coating layer remains amorphous and has no side effects on the structure of NMC during the coating process. Elementary mapping analysis, presented in Figure 2e−g, further confirms the homogeneous coating of LLSTO on NMC. Furthermore, after a thinning process on NMC-LLSTO with focused ion beam, the transmission electron microscopy (TEM) image (Figure 2h) and corresponding elementary mapping (Figure 2i) in the cross-section view show that the thickness of the LLSTO coating is around 15−20 nm. The existence of peaks that belong to Ti, La, and Sr in the energy dispersive spectrum (EDS) further certified the composition of the layered coating as LLSTO (Figure 2j). The ionic conductivity of the amorphous LLSTO is around 8.4×10^{-5} S cm^{-1} at 30 °C, which is measured with the same method described in previous work (Figure S1).[25]

The application of high voltage cathode is highly dependent on the electrochemical stability window (ESW) of SEs. For a long time, SEs were believed to have a wide stability window of 0−5 V from cyclic voltammetry (CV) measurements based on the Li/SE/Pt setup. However, much work in experiment and theory has proved their rather narrow ESW, especially the thiophosphate-based SEs.[26] High-crystalline argyrodite Li_6PS_5Cl was prepared (Figure S2a) and utilized as the SE for ASLBs, which exhibits a high ionic conductivity of 2×10^{-3} S cm^{-1} at room temperature. As shown in Figure S2b, we fitted the raw data with an equivalent circuit consisting of two parallel constant phase elements (CPEs)/resistors, represent-

DOI: 10.1021/acs.nanolett.9b02678
Nano Lett. XXXX, XXX, XXX−XXX

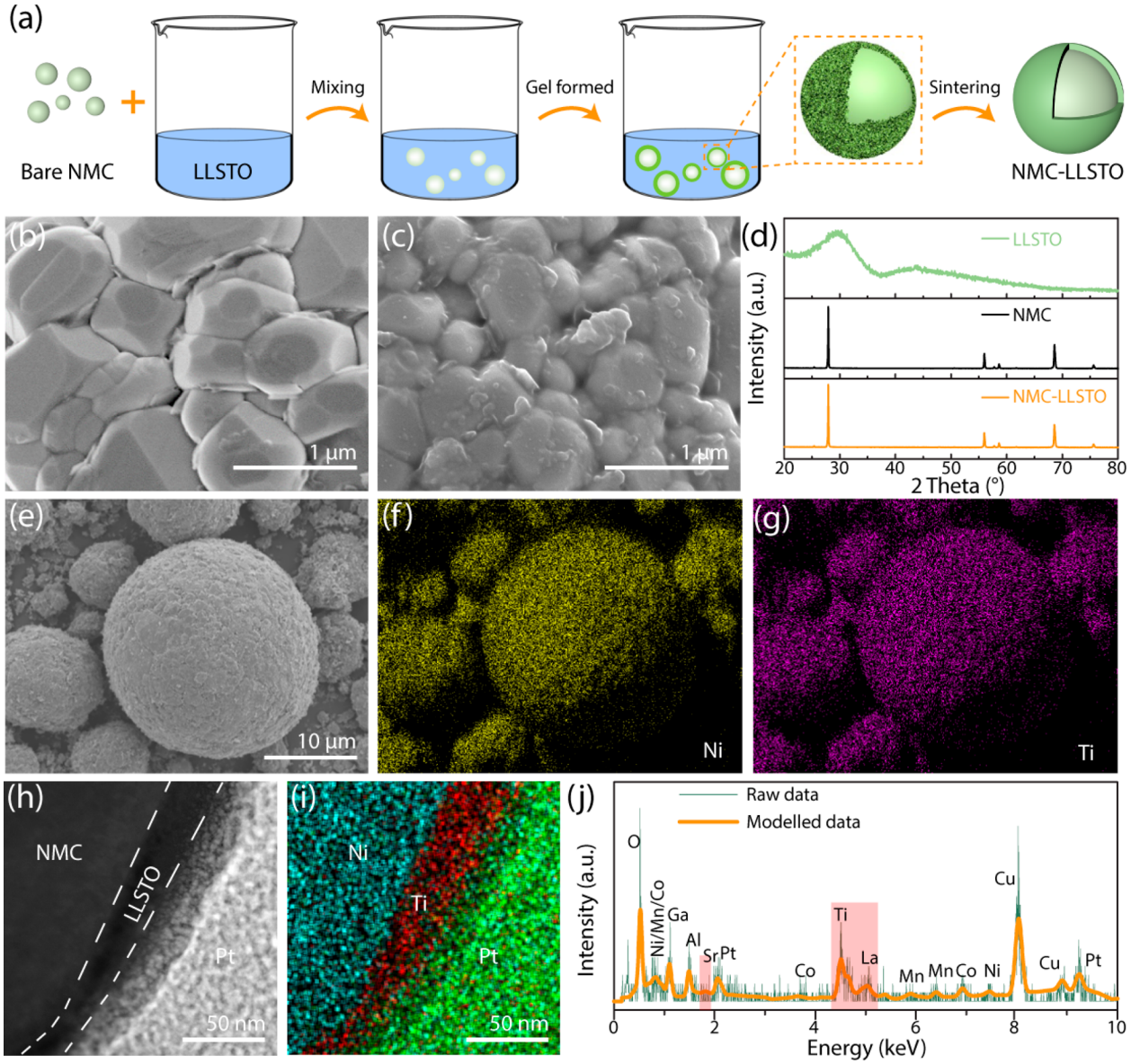

Figure 2. (a) Schematic of the process with wet chemical approach to coat LLSTO on NMC. Surface SEM images of (b) bare NMC, and (c) NMC-LLSTO. (d) XRD of NMC, LLSTO, and NMC-LLSTO. (e–g) SEM image and elemental mapping of Ni and Ti of the NMC-LLSTO. (h) TEM image, (i) elemental mapping, and (j) EDX spectrum of NMC-LLSTO to show the presence of Sr, Ti, and La elements.

ing the bulk and grain boundary resistances, in series with a CPE, representing the blocking electrodes. The resulting bulk resistance is 67 ± 1 Ω, which is in accordance with the inception value directly read from the alternating current (ac) impedance. The small semicircle represents the low grain boundary resistance. The steep linear spike at low frequencies indicates a behavior of typical ionic conductor.

Furthermore, we investigated the in situ behavior of the Li_6PS_5Cl at high voltage with the assistance of Raman spectroscopy. Figure 3a illustrates the cell setup for the Raman investigation. To amplify the decomposition signal of SE for better detection, SE mixed with carbon was chosen as the cathode material. A transparent glass window was employed to seal the cell and allow the laser to transmit. CV measurement was performed between 3.0 to 4.5 V (vs Li^+/Li), which is a typical working range of a high voltage cathode (Figure 3b). It is obvious that drastic oxidation occurs starting at around 2.3 V. This result agrees well with the thermodynamic onset of oxidation calculated to occur at 2.34 V, as obtained by first-principles thermodynamic calculations (Figure 3d).[14] Several oxidation peaks located at around 3.0, 3.6, and 4.0 V are also detected. It is interesting that there are no reduction peaks during the discharge process and no further oxidation occurred in the following cycles which suggests that the degradation products are electrochemically stable in this voltage range. Figure 3c shows the Raman spectra of the Li_6PS_5Cl at different charged potentials from 2.55 to 4.0 V. Initially, peaks located at 203, 269, 428, 577, and 602 cm^{-1} are attributed to the tetrahedral PS_4^{3-} unit in argyrodite-type Li_6PS_5Cl.[27,28] During charging, all of these peaks gradually vanished, suggesting the decomposition of Li_6PS_5Cl. As a result, newborn peaks at 156, 223, and 476 cm^{-1} are assigned to the S—S bond in Li polysulfide and sulfur which confirm the peaks in the CV coming from the gradual oxidation of S^{2-} to sulfur[29] and agree with thermodynamic calculations of the phase equilibria as voltage increased (Figure 3d). Both Li

DOI: 10.1021/acs.nanolett.9b02678
Nano Lett. XXXX, XXX, XXX−XXX

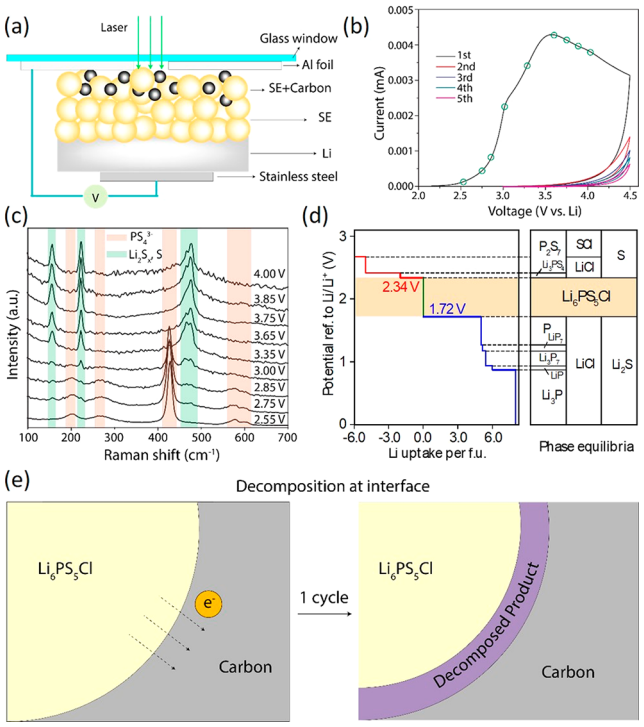

Figure 3. Investigation of the stability of Li_6PS_5Cl at the oxidation process. (a) Schematic of the cell setup for in situ Raman measurement. (b) CV curves in the first five cycles. (c) Raman spectra in different oxidation process. (d) First-principles computation results of the voltage profile and the phase equilibria of Li_6PS_5Cl solid electrolyte upon lithiation and delithiation. (e) Degradation of Li_6PS_5Cl at the interface with carbon.

polysulfide and sulfur have poor electronic and ionic conductivities, serving as passivation layers which avoid further degradation of Li_6PS_5Cl after the first cycle. This result explains why no oxidation peaks appear in the following cycles. The decomposition of Li_6PS_5Cl at high voltage is depicted in Figure 3e. Because of the addition of carbon, the electronic conductivity of the entire cathode is greatly enhanced, which can accelerate the oxidation of S^{2-} in Li_6PS_5Cl at high voltage. As a result, a layer of decomposed products is formed at the interface between the Li_6PS_5Cl and carbon. We conclude that Li_6PS_5Cl is unstable at high voltage (>3 V), whereas the corresponding products at the interface kinetically inhibit further reaction to some extent. However, due to the poor ionic conductivity the decomposed products increase the ion transport resistance in the cathode which sacrifices the cell performance. Therefore, an interface layer can effectively stabilize SEs at high voltage, and it is desired with high ionic conductivity but electron insulation.[14,30]

To further verify the significance of the interface engineering, the electrochemical performance of bare NMC and NMC-LLSTO is explored in ASLBs. In the cathode part, to eliminate the degradation caused by carbon, there are no conductive additives. Li−In is selected as the anode to avoid the side reaction between Li_6PS_5Cl and Li metal. After assembled, all ASLB testings are performed at room temperature. Figure 4a,b compares the charge and discharge profiles of bare NMC and NMC-LLSTO in the first three cycles at C/10, respectively. In the initial charging process, bare NMC exhibits a much higher overpotential than NMC-LLSTO, which can be due to the interface impedance caused by slight chemical reactions between NMC and Li_6PS_5Cl and the space charge layer effect. During cycling, the LLSTO layer could effectively avoid the decomposition of Li_6PS_5Cl and the reaction with NMC. As a result, NMC-LLSTO delivers a high discharge specific capacity of 130 mAh g^{-1}, whereas bare NMC only shows that of 80 mAh g^{-1}. The initial Coulombic efficiency is also increased from 61% to 76%. In the following cycles, it is obvious that there is significant overpotential increase (highlighted in Figure 4a) in bare NMC compared with the first charging process which comes from the increased interface resistance caused by the decomposed products in the first cycle. In contrast, this phenomenon is successfully eliminated in NMC-LLSTO (highlighted in Figure 4b). Nyquist plots of the ASLBs with bare NMC and NMC-LLSTO as cathodes after the first cycle are compared in Figure 4c. Before cycling, both electrodes show imcomplete semicircles followed by the Warburg tails, where the higher slope in the bare NMC electrode suggests relatively sluggish ion diffusion. After one cycle, the depressed semicircles are clear, and the bare NMC electrode exhibits a much larger amplitude than NMC-LLSTO which confirmed the formation of high-resistance interface layer in bare NMC.

Other conditions, such as the coating thickness and particle size of NMC, also affect the performance greatly. Figure S6 compared the full cell performances of these NMCs with different coating thicknesses. The thinner coating has an inconspicuous improvement when compared with the bare NMC. However, there is an additional oxidation plateau observed at around 1.6 V when the coating layer is thick, which can be attributed to the reaction of crystallized LLSTO. These results confirm that the coating layer with a moderate thickness (∼15−20 nm in this work) contributes to the best performance. We also compared the performance of NMC with different dimensions. A ball mill was used to adjust the NMC particle size and achieve a uniform mixture. From our data, we concluded the morphology of the NMC can be destroyed to some extent. After ball milling, the secondary particles of NMC are pulverized poorly, which exhibits poor performance even with coating (Figure S7). To protect the second particles of NMC, moderate ball milling or even manually mixing in mortar are suggested in the preparation of NMC in full cell.

Galvanostatic intermittent titration technique (GITT) is conducted to investigate the effect of coating on solid phase diffusion kinetics in the cathode. Figure 4d compares the transient discharge voltage profiles of bare NMC and NMC-LLSTO. After introducing the LLSTO coating, the polarization is significantly lowered in the whole range and a high discharge capacity of 156 mAh g^{-1} is obtained which confirmed the enhanced Li-ion diffusion. Figure 4e shows the Li-ion diffusion coefficient (D_s) of bare NMC and NMC-LLSTO in different states of Li-ion intercalation (x) of $Li_x(Ni_{1/3}Mn_{1/3}Co_{1/3})O_2$ ($0 \le x \le 0.6$). The D_s is calculated by simplified Fick's law, which is introduced in Figure S3.[29] The NMC-LLSTO exhibits greatly enhanced D_s in the range of about $0.1-10 \times 10^{-10}$ cm^2 s^{-1}, which is about five times higher than that of bare NMC. The enhanced ion diffusion in cathode can be concluded to the high ion conductivity of the LLSTO coating. In contrast, bare NMC suffers from the poor ion diffusion because of the passivated decomposed products at the interface.

Figure 4f shows the long-term cycling performances of bare NMC and NMC-LLSTO at C/3. Both cells are measured at C/10 for 4 cycles initially. The NMC-LLSTO displays a remarkable specific capacity of 107 mAh g^{-1} with an ultrastable cycling for 850 cycles with a capacity retention as high as

DOI: 10.1021/acs.nanolett.9b02678
Nano Lett. XXXX, XXX, XXX−XXX

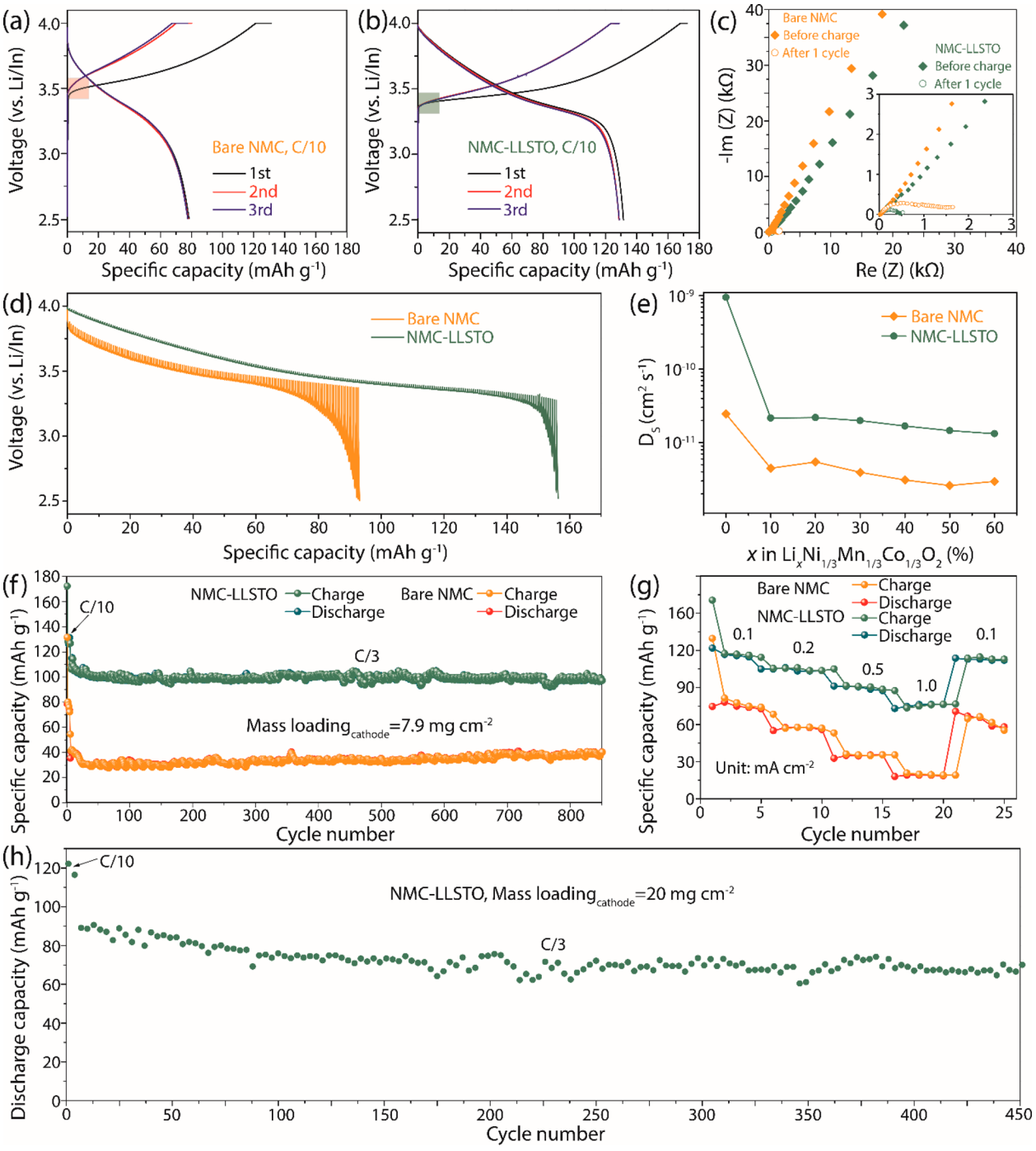

Figure 4. Electrochemical performance of ASLBs with bare NMC and NMC-LLSTO cathodes. The charge/discharge profiles of (a) bare NMC and (b) NMC-LLSTO in the initial three cycles at C/10. The comparison in overpotential after one cycle is highlighted. (c) The Nyquist plots of bare NMC and NMC-LLSTO before and after one cycle. The inset shows the magnified plots. (d) Transient voltage profiles and (e) diffusion coefficient versus depth of discharge of bare NMC and NMC-LLSTO. (f) Long-term cycling performance of bare NMC and NMC-LLSTO with mass loading of 7.9 mg cm^{-2} at C/3. (g) Rate performance of bare NMC and NMC-LLSTO. (h) Cycling performance of NMC-LLSTO with high mass loading of 20 mg cm^{-2} at C/3. All ASLBs are performed in room temperature.

91.5%. In contrast, bare NMC cathode shows poor cycling capacity of 30 mAh g^{-1}. It should be noted that the little vibration of capacity during cycling is caused by the environmental temperature variation. The outstanding cycling performance of NMC-LLSTO cathode confirms LLSTO is highly stable during charge/discharge process. It is no surprise that bare NMC also exhibits good cycling stability, because the passivated layer at the interface could stop the continuous reaction, as aforementioned. However, it significantly sacrifices the capacity of the NMC. Figure 4g compares the rate performances of bare NMC and NMC-LLSTO at 0.1, 0.2, 0.5, and 1.0 mA cm^{-2}. NMC-LLSTO exhibits high capacity of 75 mAh g^{-1} at 1.0 mA cm^{-2} (corresponding to 1.2 C), while the bare NMC shows very low capacity of 15 mAh g^{-1}. The charge/discharge profiles of both ASLBs in different rates are shown in Figure S8. When increasing the mass loading of

DOI: 10.1021/acs.nanolett.9b02678
Nano Lett. XXXX, XXX, XXX−XXX

cathode to 20 mg cm^{-2}, the NMC-LLSTO still delivers a high discharge initial capacity of 122 mAh g^{-1} at C/10, and 90 mAh g^{-1} at C/3 and keep stable for 450 cycles. So far, the significantly improved electrochemical performances of NMC-LLSTO directly stem from the interface engineering, which effectively prevented the reaction between NMC and Li_6PS_5Cl, and stabilized Li_6PS_5Cl to 4.0 V (vs Li/In) and enhances the ion diffusion in the cathode.

This improved interface stability of NMC-LLSTO compared to bare NMC with Li_6PS_5Cl solid electrolyte is also confirmed by the first-principles thermodynamic calculations (Figure 5).

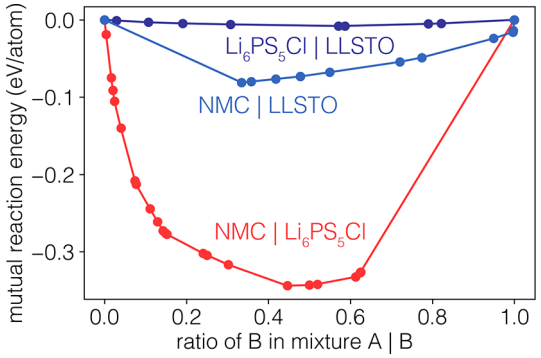

Figure 5. Calculated mutual reaction energies of the bare NMC-Li_6PS_5Cl, NMC-LLSTO, and LLSTO-Li_6PS_5Cl interfaces. The most exothermic mutual reaction energy is between the bare NMC and Li_6PS_5Cl, whereas the interfaces with LLSTO are more stable with much less favorable reaction energies.

The interfaces between NMC and Li_6PS_5Cl, NMC and LLSTO, and Li_6PS_5Cl and LLSTO were evaluated as a pseudobinary of the two contacting materials with the same scheme used in previous studies.[31] Full details on the calculations are provided in the Experimental Section. The calculations found that the interface between bare NMC and Li_6PS_5Cl has poor stability, showing a significant decomposition energy of −0.34 eV/atom. In contrast, the interface between LLSTO and NMC is much more stable, and the most stable interface is between LLSTO and Li_6PS_5Cl, which shows a negligible reaction energy. These calculation results confirm the LLSTO coating improves the thermodynamic interface stability between NMC and Li_6PS_5Cl.

Table S2 summarized and compared the electrochemical performance of reported ASLBs using $LiNi_{1/3}Mn_{1/3}Co_{1/3}O_2$ as the cathode and metal sulfide as the electrolyte.[32−37] Our ASLBs with interface engineering exhibit the longest cycling ever reported in the literature. It should be noted that in some of these works conductive carbon additives are applied in the cathode, which may optimize the performance to some extent. In our work, we only focused on the interface stabilization between the cathode and Li_6PS_5Cl. We believe our interface engineering approach is universal and can be implemented in a wide range of high-energy cathodes. We believe the performance of the ASLBs can be further improved if a cathode with higher capacity is used, such as $LiCoO_2$ and high-Ni content NMC ($LiNi_{0.8}Mn_{0.1}Co_{0.1}O_2$).

In conclusion, we demonstrated an interface engineering on NMC with a thin layer of highly ionic conductive and amorphous LLSTO coating to stabilize the interface between NMC and Li_6PS_5Cl in ASLBs. The decomposition of Li_6PS_5Cl in high oxidation voltage is in situ investigated through Raman and the decomposed products at the interface, such as polysulfide and sulfur, are revealed to possess poor ionic conductivity, which caused high interface resistance. Therefore, with the protection of amorphous LLSTO, the decomposition is effectively eliminated. Compared with other reported coating materials with ionic conductivity ranging from 10^{-9} to 10^{-6} S cm^{-1}, the interface layer introduced in this work exhibits excellent ionic conductivity of 8.4×10^{-5} S cm^{-1} at 30 °C, which benefits the reaction kinetic and interface stability. Meanwhile, the amorphous coating promoted the interface contact and minimized the interface resistance between different layers. The superior interface stability enabled all solid NMC-LLSTO/Li_6PS_5Cl/Li−In cells with highly stable cycling performance (850 cycles with capacity retention of 91.5%) at C/3 in room temperature. The mutual reaction energy at the interface of NMC-Li_6PS_5Cl, NMC-LLSTO, and LLSTO-Li_6PS_5Cl is revealed through first-principles thermodynamic calculations. This interface engineering approach at nanometer scale can potentially be applied to other high-voltage cathodes, like $LiCoO_2$ and high-Ni-content NMC, which can be implemented in practical application of high energy ASLBs, especially for the cathode interface stabilization in thiophosphate-based ASLBs.

Experimental Section. *Materials Synthesis and Preparation. LLSTO Sol Preparation.* LLSTO solution is prepared based on our previous publication.[25] Lanthanum 2-methoxyethoxide (Alfa Aesar, 99.9%, 5% w/v in 2-methoxyethanol.), titanium isopropoxide (Aldrich, 99.9%), lithium isopropoxide (Alfa Aesar, 99.9%), and strontium isopropoxide (Sigma-Aldrich, 99.9%) are utilized as original chemicals. Briefly, lithium isopropoxide, lanthanum 2-methoxyethoxide, titanium isopropoxide, and strontium isopropoxide were mixed in a glovebox according to the stoichiometric ratio of $Li_{0.35}La_{0.50}Sr_{0.05}TiO_3$ (LLSTO), and 10% in mole excess lithium isopropoxide was added in order to compensate the loss during annealing. After refluxing for 2 h in Ar atmosphere, 10 mol % water was added into the system to accelerate the following gel formation.

Coating LLSTO on NMC 111. NMC powder was baked at 80 °C in vacuum oven for 8 h, which can prevent coating nonuniformity caused by water absorbed in NMC particles. Then the dried powder was mixed in the solution of LLSTO at a certain ratio (1 g NMC/0.25 mmol LLSTO). The suspension was stirred for 2 h in air in order to achieve uniform mixing. Afterward, the suspension was placed in the fume hood and to wait for gel formation. Then the gel was calcined in the furnace at 380 °C for 2 h in air to remove organic residues; then the temperature was raised to 500 °C for another 10 min in order to achieve full sintering. At last, the LLSTO-coated NMC 111 was ground for 10 min.

Li_6PS_5Cl Preparation. Argyrodite Li_6PS_5Cl was synthesized in a typical high-energy mechanical ball milling method and subsequent annealing treatment. A stoichiometric mixture of Li_2S (Sigma-Aldrich, 99.98%), P_2S_5 (Sigma-Aldrich, 99%), and LiCl (Sigma-Aldrich, 99%) was milled in a stainless steel vacuum jar (50 mL) with 20 stainless steel balls (6 mm in diameter) for 10 h at 500 rpm under an argon atmosphere. Next, the mixture was sealed in a glass tube under argon atmosphere and annealed in a quartz tube furnace at 550 °C for 6 h.

Materials Characterization. X-ray diffraction (XRD) measurements were carried out with X'Pert PRO system (PANalytical, Germany) with Cu Kα as the radiation source.

DOI: 10.1021/acs.nanolett.9b02678
Nano Lett. XXXX, XXX, XXX−XXX

The SEM images and EDS mapping were characterized with SEM (JEOL JSM 7000F). The thinner process of the NMC-LLSTO sample was performed on a high-resolution SEM/FIB-FEI Scios DualBeam system. TEM and EDS mapping images were collected on the Cs-corrected TEM/STEM-FEI Titan Themis 300. Raman spectra were measured on a Thermo Scientific DXR with 532 nm laser excitation.

Electrochemistry Evaluation. Ionic Conductivity of LLSTO. LLSTO sol was prepared following the standard procedure[1] then spin-coated on R-plane ($1\bar{1}02$) sapphire substrates at 3000 rpm (rpm) for 30 s in ambient air. Then the gel film was dried at 80 °C for 30 min on a hot plate. In addition, the dried gel films were fired at 380 °C. In order to achieve a certain thickness (300 nm), this procedure may be repeated several times. The thin film was annealed at 450 °C for 7 min in order to obtain the optimum ionic conductivity based on our previous work.

The ionic conductivity tests were conducted with electrochemical impedance spectroscopy (EIS) at Ar atmosphere. For the EIS measurement, two parallel slits of Au electrodes were sputtered on LLSTO thin films with a mask and vacuum deposition method. The test was manipulated in a Split Test Cell (MTI) which was assembled in a glovebox to avoid moisture absorption. The impedance was measured from 200 kHz to 0.1 Hz using a 100 mV ac signal by a galvanostat/potentiostat/impedance analyzer (Biologic VMP3) with a low current board. Impedance data evaluation and simulation are obtained by Z fit simulation.

Ionic Conductivity of Li_6PS_5Cl. The ionic conductivity of Li_6PS_5Cl was measured using EIS by an ion-blocking symmetric system. In brief, 200 mg of grounded Li_6PS_5Cl powder was cold-pressed under 300 MPa into a pellet (0.45 mm in thickness, 12.7 mm in diameter). After that, two pieces of indium foil (11.1 mm in diameter) were pressed onto both sides of the pellet under 50 MPa. The as-prepared In/Li_6PS_5Cl/In pellet was placed in a Swagelok cell for EIS measurement, which was carried out at frequencies from 1 MHz to 100 mHz with ac amplitude of 50 mV by electrochemistry workstation (Biologic SP150). Impedance data evaluation and simulation are obtained by Z fit simulation.

Stability Investigation of Li_6PS_5Cl with in Situ Raman. The stability of Li_6PS_5Cl in the oxidation process was investigated with CV measurement, where the decomposition was in situ observed with Raman. The setup of the cell is schematically illustrated in Figure 4a. The cathode material composed of Li_6PS_5Cl and carbon black as a ratio of 70/30 was prepared in a ball mill method. One hundred milligrams of Li_6PS_5Cl powder was cold-pressed under 300 MPa. After that, 10 mg of cathode material was cast on the pellet with a pressure of 100 MPa. A piece of Li was utilized as the anode and pressed on the other side of the pellet. The sandwiched pellets were sealed in a three-electrode cell from EC-CELL, where a piece of glass window was used to seal the cell and allowed the laser to observe the cathode part. The CV was operated between 3.0 and 4.5 V at a scan rate of 0.1 mV s^{-1}.

Fabrication of ASLB. To prepare the cathode, NMC with/without LLSTO was manually mixed with Li_6PS_5Cl with the ratio of 70/30. One hundred milligrams of Li_6PS_5Cl was first pressed into a pellet with a diameter of 12.7 mm under 300 MPa. After that, 10 mg of as-prepared cathode was casted onto the pellet and followed pressing under a pressure of 100 MPa. The mass loading of the active material is 5.14 mg cm^{-2}. In the high mass loading cell, the mass loading of active material is 16.33 mg cm^{-2}. A piece of In−Li was pressed to the other side with a pressure of 100 MPa. Al and Cu foils were selected as the current collector in the cathode and anode, respectively. An extra pressure of 50 MPa was applied during measurement.

Rate and Cycling Performance. The rate and cycling measurements were performed with a constant current/constant voltage protocol between the cutoff voltage of 2.5 and 4.0 V (vs Li−In), that is, the cells were charged at the constant current to 4.0 V and then held at 4.0 V for 1 h, following being discharged to 2.5 V at constant current. The current for the rate measurement was based on the area of the SSE pellet, that is, 1/2 in. diameter. For the long-term cycling, the cell was cycled at C/10 for five cycles, and then cycled at C/3. Here 1C means 160 mA/g based on the weight of active material in the cathode.

GITT Measurement. All the cells were first charged for 5 min at constant current of C/20 and rested for 10 min until the voltage reached 4.0 V and then discharged for 5 min at constant current of C/20 and rested for 10 min until the voltage reached 2.5 V.

Computation. The thermodynamic electrochemical window of Li_6PS_5Cl was calculated as in previous studies[31] using material energies obtained from the Materials Project (MP) database[38] and queried using the "pymatgen package".[39] The voltage profile and phase equilibria of Li_6PS_5Cl was calculated by constructing a grand potential phase diagram, which identifies the phase equilibria of the material in equilibrium with an open reservoir of Li with chemical potential μ_{Li}. The chemical potential was considered as a function of applied potential φ using the relation $\mu_{Li}(\varphi) = \mu^0_{Li} - e\varphi$, where μ^0_{Li} is the chemical potential of Li metal, and φ is referenced to Li metal, as in previous studies.[40,41] For the interface stability calculations, we considered the interface as a pseudobinary of the two materials in contact using the same approach as defined in previous work.[31] Using this method, at any mixing ratio between the two phases, given by a linear combination of the two parent phases normalized to one atom per formula unit, the set of phases which corresponds to the lowest energy can be identified. The mutual reaction energy is found by calculating the difference between the energy of the phase equilibria and the energy of the pseudobinary at a given mixing ratio, using the same approach as defined in our previous work.[31]

■ ASSOCIATED CONTENT

Supporting Information

The Supporting Information is available free of charge on the ACS Publications website at DOI: 10.1021/acs.nanolett.9b02678.

Additional experimental and figures including Nyquist plot of LLSTO, XRD patterns of Li_6PS_5Cl and ionic conductivity, diffusion calculation, optimization of coating conditions, morphology of NMC with different coating thickness, electrochemical performance of NMC with different coating thickness, morphology of NMC after ball mill and the corresponding electrochemical performance, galvanic charge/discharge profiles in rate measurement, calculated thermodynamic decomposition energies and phase equilibria (PDF)

DOI: 10.1021/acs.nanolett.9b02678
Nano Lett. XXXX, XXX, XXX−XXX

AUTHOR INFORMATION

Corresponding Authors

*E-mail: h.zhu@neu.edu (H.Z.).
*E-mail: yanwang@wpi.edu (Y.W.).
*E-mail: yfmo@umd.edu (Y.M.).

ORCID

Yifei Mo: 0000-0002-8162-4629
Yan Wang: 0000-0003-1060-2956
Hongli Zhu: 0000-0003-1733-4333

Author Contributions

‖D.C. and Y. Z. contributed equally to this work.

Notes

The authors declare no competing financial interest.

ACKNOWLEDGMENTS

H.Z. acknowledges the financial support from Northeastern Tier 1, National Science Foundation CBET-1924534, and Rogers Corporation. H.Z. acknowledges the Kostas Nanomanufacturing Research Center for sharing the scanning electron microscope. Y.W. and Y.Z. acknowledges the financial support by NSF DMR- 1608398. The authors thank Dr. Joshua Gallaway in Chemical Engineering in Northeastern University for the sharing of Raman measurement. Y.M. acknowledges the financial support from National Science Foundation under award no. 1550423 and the computational facilities from the University of Maryland supercomputing resources and the Maryland Advanced Research Computing Center (MARCC).

REFERENCES

(1) Janek, J.; Zeier, W. G. *Nature Energy* **2016**, *1*, 16141.
(2) Manthiram, A.; Yu, X.; Wang, S. *Nature Reviews Materials* **2017**, *2*, 16103.
(3) Meesala, Y.; Jena, A.; Chang, H.; Liu, R.-S. *ACS Energy Letters* **2017**, *2* (12), 2734−2751.
(4) Yue, J.; Yan, M.; Yin, Y.-X.; Guo, Y.-G. *Adv. Funct. Mater.* **2018**, *28* (38), 1707533.
(5) Kato, Y.; Hori, S.; Saito, T.; Suzuki, K.; Hirayama, M.; Mitsui, A.; Yonemura, M.; Iba, H.; Kanno, R. *Nature Energy* **2016**, *1*, 16030.
(6) Choi, J. W.; Aurbach, D. *Nature Reviews Materials* **2016**, *1*, 16013.
(7) Chen, S.; Xie, D.; Liu, G.; Mwizerwa, J. P.; Zhang, Q.; Zhao, Y.; Xu, X.; Yao, X. *Energy Storage Materials* **2018**, *14*, 58−74.
(8) Han, F.; Yue, J.; Chen, C.; Zhao, N.; Fan, X.; Ma, Z.; Gao, T.; Wang, F.; Guo, X.; Wang, C. *Joule* **2018**, *2* (3), 497−508.
(9) Zhou, W.; Wang, Z.; Pu, Y.; Li, Y.; Xin, S.; Li, X.; Chen, J.; Goodenough, J. B. *Adv. Mater.* **2019**, *31* (4), 1805574.
(10) Strauss, F.; Bartsch, T.; de Biasi, L.; Kim, A. Y.; Janek, J.; Hartmann, P.; Brezesinski, T. *ACS Energy Letters* **2018**, *3* (4), 992−996.
(11) Cui, S.; Wei, Y.; Liu, T.; Deng, W.; Hu, Z.; Su, Y.; Li, H.; Li, M.; Guo, H.; Duan, Y.; Wang, W.; Rao, M.; Zheng, J.; Wang, X.; Pan, F. *Adv. Energy Mater.* **2016**, *6* (4), 1501309.
(12) Takada, K.; Ohno, T.; Ohta, N.; Ohnishi, T.; Tanaka, Y. *ACS Energy Letters* **2018**, *3* (1), 98−103.
(13) Park, K. H.; Bai, Q.; Kim, D. H.; Oh, D. Y.; Zhu, Y.; Mo, Y.; Jung, Y. S. *Adv. Energy Mater.* **2018**, *8* (18), 1800035.
(14) Zhu, Y.; He, X.; Mo, Y. *ACS Appl. Mater. Interfaces* **2015**, *7* (42), 23685−23693.
(15) Jena, A.; Meesala, Y.; Hu, S.-F.; Chang, H.; Liu, R.-S. *ACS Energy Letters* **2018**, *3* (11), 2775−2795.
(16) Noh, S.; Nichols, W. T.; Cho, M.; Shin, D. *J. Electroceram.* **2018**, *40* (4), 293−299.
(17) Han, F.; Zhu, Y.; He, X.; Mo, Y.; Wang, C. *Adv. Energy Mater.* **2016**, *6* (8), 1501590.
(18) Ohta, N.; Takada, K.; Zhang, L.; Ma, R.; Osada, M.; Sasaki, T. *Adv. Mater.* **2006**, *18* (17), 2226−2229.
(19) Zhang, J.; Zhong, H.; Zheng, C.; Xia, Y.; Liang, C.; Huang, H.; Gan, Y.; Tao, X.; Zhang, W. *J. Power Sources* **2018**, *391*, 73−79.
(20) Seino, Y.; Ota, T.; Takada, K. *J. Power Sources* **2011**, *196* (15), 6488−6492.
(21) Sakuda, A.; Hayashi, A.; Tatsumisago, M. *Chem. Mater.* **2010**, *22* (3), 949−956.
(22) Yubuchi, S.; Ito, Y.; Matsuyama, T.; Hayashi, A.; Tatsumisago, M. *Solid State Ionics* **2016**, *285*, 79−82.
(23) Culver, S. P.; Koerver, R.; Zeier, W. G.; Janek, J. *Adv. Energy Mater.* **2019**, *9* (24), 1900626.
(24) Jung, S. H.; Oh, K.; Nam, Y. J.; Oh, D. Y.; Brüner, P.; Kang, K.; Jung, Y. S. *Chem. Mater.* **2018**, *30* (22), 8190−8200.
(25) Zhang, Y.; Zheng, Z.; Liu, X.; Chi, M.; Wang, Y. *J. Electrochem. Soc.* **2019**, *166* (4), A515−A520.
(26) Auvergniot, J.; Cassel, A.; Ledeuil, J.-B.; Viallet, V.; Seznec, V.; Dedryvère, R. *Chem. Mater.* **2017**, *29* (9), 3883−3890.
(27) Sang, L.; Haasch, R. T.; Gewirth, A. A.; Nuzzo, R. G. *Chem. Mater.* **2017**, *29* (7), 3029−3037.
(28) Rosero-Navarro, N. C.; Miura, A.; Tadanaga, K. *J. Sol-Gel Sci. Technol.* **2019**, *89* (1), 303−309.
(29) Hagen, M.; Schiffels, P.; Hammer, M.; Dörfler, S.; Tübke, J.; Hoffmann, M. J.; Althues, H.; Kaskel, S. *J. Electrochem. Soc.* **2013**, *160* (8), A1205−A1214.
(30) Nolan, A. M.; Zhu, Y.; He, X.; Bai, Q.; Mo, Y. *Joule* **2018**, *2* (10), 2016−2046.
(31) Zhu, Y.; He, X.; Mo, Y. *J. Mater. Chem. A* **2016**, *4* (9), 3253−3266.
(32) Chida, S.; Miura, A.; Rosero-Navarro, N. C.; Higuchi, M.; Phuc, N. H. H.; Muto, H.; Matsuda, A.; Tadanaga, K. *Ceram. Int.* **2018**, *44* (1), 742−746.
(33) Sakuda, A.; Takeuchi, T.; Kobayashi, H. *Solid State Ionics* **2016**, *285*, 112−117.
(34) Kitaura, H.; Hayashi, A.; Tadanaga, K.; Tatsumisago, M. *Electrochim. Acta* **2010**, *55* (28), 8821−8828.
(35) Machida, N.; Kashiwagi, J.; Naito, M.; Shigematsu, T. *Solid State Ionics* **2012**, *225*, 354−358.
(36) Okada, K.; Machida, N.; Naito, M.; Shigematsu, T.; Ito, S.; Fujiki, S.; Nakano, M.; Aihara, Y. *Solid State Ionics* **2014**, *255*, 120−127.
(37) Asano, T.; Yubuchi, S.; Sakuda, A.; Hayashi, A.; Tatsumisago, M. *J. Electrochem. Soc.* **2017**, *164* (14), A3960−A3963.
(38) Jain, A.; Ong, S. P.; Hautier, G.; Chen, W.; Richards, W. D.; Dacek, S.; Cholia, S.; Gunter, D.; Skinner, D.; Ceder, G.; Persson, K. A. *APL Mater.* **2013**, *1* (1), 011002.
(39) Ong, S. P.; Richards, W. D.; Jain, A.; Hautier, G.; Kocher, M.; Cholia, S.; Gunter, D.; Chevrier, V. L.; Persson, K. A.; Ceder, G. *Comput. Mater. Sci.* **2013**, *68*, 314−319.
(40) Mo, Y.; Ong, S. P.; Ceder, G. *Chem. Mater.* **2012**, *24* (1), 15−17.
(41) Ong, S. P.; Wang, L.; Kang, B.; Ceder, G. *Chem. Mater.* **2008**, *20* (5), 1798−1807.

DOI: 10.1021/acs.nanolett.9b02678
Nano Lett. XXXX, XXX, XXX−XXX